Gradient-excitation encoding combined with frequency and phase encodings for three-dimensional ultra-low-field MRI

Juhani Dabek[1], Koos C. J. Zevenhoven[1], Jaakko O. Nieminen[1], Panu T. Vesanen[1],
Raimo Sepponen[2] and Risto J. Ilmoniemi[1]

Abstract— Ultra-low-field magnetic resonance imaging (ULF MRI) in microtesla fields is a new technology with features unseen in tesla-range MRI. Instead of induction coils as sensors, superconducting quantum interference device (SQUID) sensors are used, providing a frequency-independent signal-to-noise ratio (SNR). Owing to its tolerance for large relative imaging-field inhomogeneities, electromagnet shimming is not necessary. ULF MRI can also be combined with magnetoencephalography (MEG) to image the brain with close to millimetre–millisecond resolution. In this paper, the hybrid MEG-MRI device developed at Aalto University will be presented, as well as a 3D imaging scheme combining gradient-excitation encoding with frequency and phase and encodings. It is noteworthy that, regarding the presented gradient-excitation encoding in ULF MRI, the kilohertz-range Larmor frequencies allow MR signals to propagate unattenuated through tissue, which is not the case in tesla-range MRI with Larmor frequencies even above 100 MHz. Thus, the presented encoding method is especially compatible with ULF MRI, where the use of three different encoding mechanisms for three-dimensional imaging is possible. The feasibility of image reconstruction with the gradient-excitation-encoding method is demonstrated by simulations.

I. INTRODUCTION

In traditional magnetic resonance imaging (MRI), ever higher fields, *i.e.* far above 1 T, are pursued to enhance the signal-to-noise ratio (SNR) and to shorten imaging times. However, the use of ultra-low fields (ULF) around 50 µT opens new possibilities: the system can have an open geometry without a magnet bore, coil shimming is not necessary, the device can be less expensive than a high-field counterpart, T_1 contrast is enhanced, as has been shown by the pioneering work of John Clarke and his group [1], and magnetoencephalography (MEG) can be incorporated into the same device. The first multichannel 3D ULF-MRI brain images, from a sheep brain, were produced by the Los Alamos group in the USA [2]. While ULF MRI provides structural brain images with a spatial resolution of a few mm with current state-of-the-art, MEG observes cortical activity with ms time resolution [3]. In ULF MRI, the low Larmor frequencies $f_0 \sim 1$ kHz let the MR signals propagate unattenuated through tissue because of negligible tissue eddy currents or molecular coupling mechanisms [4]. A key technique in ULF MRI is using a prepolarizing field of the order of $10 - 100$ mT to enhance the SNR. Working

[1]Department of Biomedical Engineering and Computational Science, Aalto University School of Science, P. O. Box 12200, FI-00076 AALTO, Finland `juhani.dabek at aalto.fi`

[2]Department of Electronics, Aalto University School of Electrical Engineering

Fig. 1. Aalto University MEG-MRI device. The aberration is caused by the used fisheye lens.

hybrid MEG-MRI devices have been built in Los Alamos [5] and at Aalto University, Finland [6] (see Fig. 1).

In this article, the gradient-excitation-encoding method together with frequency and phase encodings, is presented with 3D image-reconstruction simulations. The new method is somewhat similar to the prior polarization-encoding method, also applicable in ULF MRI [7]; in the latter, both the amplitude and the phase are encoded, but in the former only the amplitude of MR signals. In higher fields, similar methods have existed for a longer time, such as using a wavelet basis for the encoding [8], or optimizing the use of encoding fields by the singular value decomposition (SVD) [9]. Imaging even without gradients in the measurement field has been demonstrated, making use of phase gradients generated by RF fields [10]. In the following, the basis of ULF MRI, which may be combined with current MEG

devices, is briefly described. Then the new encoding and 3D-imaging methods are introduced, validated by simulations.

A. Hybrid MEG-MRI featuring ULF MRI

The sensors of choice for MEG are based on superconducting quantum interference device (SQUID) technology. SQUID sensors can measure magnetic fields above 1 Hz with very low noise (around 1 fT/Hz$^{-1/2}$). In the Aalto University setup, planar modules with one magnetometer and two orthogonal gradiometers are used [6]. ULF-MRI signals and fT-level MEG, and the sensitivity of the SQUID sensors necessitate a magnetically shielded room (MSR) for attenuating the ambient noise fields at DC and near DC (mu-metal sheets) and AC (aluminium sheets). Specific hardware solutions are also needed to run ULF-MRI sequences, as will be seen below.

As the prepolarizing field $B_p \sim 20$ mT is ramped down in a few ms, eddy currents are induced in the MSR walls, which may lead to significant artefacts in acquired MEG or ULF-MRI signals [11]. At Aalto University, this problem has been solved by constructing a self-shielded B_p coil [12]. In addition, the SQUID sensors are protected against B_p by placing flux dams (Josephson junctions) in series with the pickup loop and niobium plates above and below the SQUID chips [13]. For the stability of the imaging field $B_0 \sim 50$ μT and the frequency-encoding gradient G_ω, their electromagnet currents are supplied from car batteries with tailored circuitry. The used gradient fields are of the order of $G \sim 130$ μT/m. The dedicated coil producing the uniform excitation field $B_1 \lesssim 40$ μT operates at $f_0 \sim 2$ kHz.

II. METHODS

With the given knowledge on ULF MRI, it is now easier to proceed to the theory that enables using three different encoding mechanisms in 3D ULF MRI, with a simulation application that should be compatible with future Aalto University MEG-MRI setup measurements. First, the basics of image formation with frequency and phase encodings and, especially, gradient-excitation encoding are presented, then extending to an image-reconstruction simulation to verify the validity of the method.

A. Image formation

Inspired by Ref. [14], the basic idea is simple: three orthogonal and uniform gradients are used such that the first one produces the frequency encoding, the second one the phase encoding and the third one the gradient-excitation encoding. The idea of the gradient-excitation encoding is to produce a spatially varying excitation pulse that modulates the amplitude of the MR signal in a controlled manner, instead of the phase as in phase encoding; the gradient-excitation field should also be orthogonal to the measurement field. Furthermore, the dedicated B_1 coil is used to produce a π pulse after the phase and gradient-excitation encodings that are applied simultaneously, resulting in an echo (see
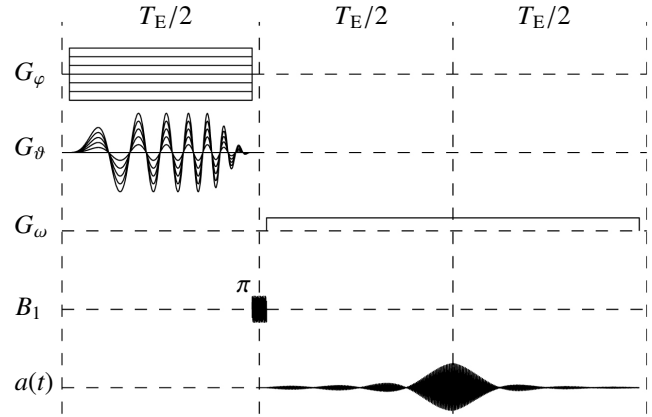

Fig. 2. Schematic simulation imaging sequence. G_φ stands for the phase encoding, G_ϑ the gradient-excitation encoding that is broadband, G_ω the frequency encoding, B_1 the dedicated-coil π pulse and $a(t)$ is the detected signal. The signals are not to scale. Just prior to the start of the schematic, the sample has been magnetized in a prepolarizing field B_p that is orthogonal to the measurement field B_0 and the G_φ and G_ω fields. The G_ϑ field is also orthogonal to B_0, and all three gradients are orthogonal to each other. B_p is switched off non-adiabatically, whence MR precession in B_0 is immediately initiated. When G_φ and G_ϑ are switched off, the π pulse from the dedicated B_1 coil produces the MR echo $a(t)$. In the process of gradient excitation, planes in the G_ϑ direction are excited in a controlled manner at each step. The planes that are excited may have voxels with magnetic moments with different phases; the excitation equivalent to a π rotation allows the voxel signal to reproduce.

Fig. 2). Retelling Ref. [15], the measured MR signal from a homogeneous voxel α is proportional to

$$b_{n,m,\alpha}(t) = e^{-t/T_{2,\alpha}} e^{-|t-T_E|/T_{2,\alpha}^+} \cos\left(\omega_\alpha t + \varphi_{n,\alpha}\right) \cos\left(\vartheta_{m,\alpha}\right), \quad (1)$$

where n is the index for the phase-encoding gradient G_φ and m for the gradient-excitation-encoding gradient G_ϑ, respectively; t the time after B_p switch-off; $T_{2,\alpha}$ the transverse relaxation time, $1/T_{2,\alpha}^+ = 1/T_{2,\alpha} - 1/T_{2,\alpha}^*$, where $T_{2,\alpha}^*$ is the inhomogeneous $T_{2,\alpha}$, all in voxel α; T_E is the time to echo; ω_α the Larmor frequency, $\vartheta_{m,\alpha}$ the tilt angle modulating the magnetization amplitude from the gradient-excitation encoding and $\varphi_{n,\alpha}$ the phase from the G_φ encoding in voxel α. At ultra-low fields, effects in the longitudinal relaxation time T_1 may prove important in brain imaging, as demonstrated by the Los Alamos group [16] but, in the simulations here, T_1 relaxation does not serve a special purpose.

Further simplifications have been made to avoid unnecessary complexity: the spin density is constant within the phantom; the lead field of the detector over the field of view (FOV) is uniform; the prepolarization duration is regarded long; B_p is homogeneous over the FOV; dephasing within voxels due to the gradients is neglected; and the dedicated-B_1-coil π pulse excites the sample uniformly.

The pulsed gradient-excitation field deserves more thought. First of all, the field must be orthogonal to the measurement field. In the Aalto University setup, e.g., this could be directly implemented by rewiring one set of the transverse gradient coils, or simply constructing a new coil pair e.g. one half above and the other half below

the FOV. To excite whole planes with the same gradient-excitation encoding, but varying phase encodings, the pulse has to be broadband. It is suggested here that in addition to amplitude modulation, the gradient-excitation pulse is frequency modulated. Implicit in the simulation, the pulse is assumed broadband (at least 110 Hz because of the phase-encoding gradient), and should be considered in practical measurements. Adjusting excitation-pulse bandwidths has been studied previously [17], [18].

Next, the frequency and phase variables in (1) will be fixed in terms of electromagnet fields, in particular B_{ω,p_ω}, B_{φ,q_φ} and $B_{\vartheta,s_\vartheta}$ described below, where the indexed representations with frequency, phase and gradient-excitation direction coordinates $(p_\omega, q_\varphi, s_\vartheta)$, respectively, are also stated to enable simulations. With a uniform measurement field B_0 and a frequency-encoding gradient field B_{ω,p_ω}, where p_ω is the coordinate index along the frequency-encoding direction,

$$\omega_{p_\omega} = 2\pi\gamma(B_0 + B_{\omega,p_\omega}) = 2\pi F_\omega(p_{\min} + p_\omega - 1) , \quad (2)$$

where γ is the gyromagnetic ratio, $(p_{\min} + P_\omega/2)F_\omega = \gamma B_0$ and P_ω is the number of planes with the different frequency encodings. For the phase encoding with a gradient field B_{φ,q_φ}, where q_φ indexes the coordinate along the phase-encoding direction,

$$\varphi_{n,q_\varphi} = 2\pi\gamma B_{\varphi,q_\varphi}\tau\frac{n - \lceil Q_\varphi/2\rceil}{Q_\varphi} = 2\pi(q_\varphi - \lceil Q_\varphi/2\rceil)\frac{n - \lceil Q_\varphi/2\rceil}{Q_\varphi}, \quad (3)$$

where τ is the duration of the phase-encoding, Q_φ is the number of phase-encoding steps and $\lceil\cdot\rceil$ denotes rounding up. Finally, the tilt angle by the gradient-excitation field with a maximum amplitude $B_{\vartheta,s_\vartheta}$ at location s_ϑ in the variation direction, is manipulated as

$$\vartheta_{m,s_\vartheta} = \pi\gamma\frac{B_{\vartheta,s_\vartheta}}{2}\tau\frac{m-1}{S_\vartheta+1} = (\pi(s_\vartheta - 1) - \psi_\vartheta)\frac{m-1}{S_\vartheta+1}, \quad (4)$$

where τ is the duration of the gradient-excitation encoding, $S_\vartheta + 1$ is the number of gradient-excitation-encoded steps, and $B_{\vartheta,s_\vartheta}$ is divided by 2 because of application of excitation from only one direction. The gradient-excitation field is zero at the voxel where $\pi(s_\vartheta - 1) = \psi_\vartheta$ holds.

Equations (2), (3) and (4) link the physical gradient fields and the numerical operation with frequencies and phases together. The phase-encoding and gradient-excitation-encoding gradients may be applied simultaneously before a uniform π pulse from the dedicated B_1 coil, and acquisition in the frequency-encoding gradient field. Eventually, the detected signal at phase-encoding n from all voxels $\alpha \,\hat{=}\, (p_\omega, q_\varphi, s_\vartheta)$ is proportional to

$$a_{n,m}(t) = \sum_{p_\omega=1}^{P_\omega}\sum_{q_\varphi=1}^{Q_\varphi}\sum_{s_\vartheta=1}^{S_\vartheta+1} b_{n,m,(p_\omega,q_\varphi,s_\vartheta)}(t) . \quad (5)$$

The voxel representation may be recovered through two Fourier transforms and solving one linear system. Starting with the frequency-encoding direction,

$$\tilde{a}_{n,m}(p_\omega) = \frac{1}{N}\sum_{n_t=0}^{N-1} a_{n,m}(n_t\Delta t)e^{-2\pi i(p_{\min}+p_\omega-1)\frac{n_t}{N}} , \quad (6)$$

where N is the number of samples, $\Delta t = 1/f_s$ is the sampling interval with sampling frequency f_s, and the frequency index is as in (2). Another transform is applied in the phase-encoding direction, *i.e.*,

$$\tilde{\tilde{a}}_m(p_\omega, q_\varphi) = \frac{1}{Q_\varphi}\sum_{n=1}^{Q_\varphi}\tilde{a}_{n,m}(p_\omega)\, e^{-2\pi(q_\varphi-\lceil Q_\varphi/2\rceil)\frac{n-\lceil Q_\varphi/2\rceil}{Q_\varphi}} , \quad (7)$$

where (3) is useful. Now, the one remaining factor in the image-reconstruction process is the gradient-excitation encoding. Continuing from the result (7) with (1) and (4),

$$\underbrace{\tilde{\tilde{a}}_m(p_\omega, q_\varphi)}_{[\tilde{\tilde{\mathbf{a}}}(p_\omega,q_\varphi)]_m} = \sum_{s_\vartheta=1}^{S_\vartheta+1}\underbrace{\tilde{\tilde{\tilde{a}}}(p_\omega, q_\varphi, s_\vartheta)}_{[\tilde{\tilde{\tilde{\mathbf{a}}}}(p_\omega,q_\varphi)]_{s_\vartheta}}\underbrace{\cos\Big((\pi(s_\vartheta - 1) - \psi_\vartheta)\frac{m-1}{S_\vartheta+1}\Big)}_{[\mathbf{C}]_{m,s_\vartheta}}, \quad (8)$$

where $\tilde{\tilde{\tilde{a}}}(p_\omega, q_\varphi, s_\vartheta)$ is the voxel-representation of the image. The equation is written in matrix form

$$\tilde{\tilde{\mathbf{a}}}(p_\omega, q_\varphi) = \mathbf{C}\tilde{\tilde{\tilde{\mathbf{a}}}}(p_\omega, q_\varphi) \quad (9)$$

which should be solved for $\tilde{\tilde{\tilde{a}}}(p_\omega, q_\varphi, s_\vartheta) = [\tilde{\tilde{\tilde{\mathbf{a}}}}(p_\omega, q_\varphi)]_{s_\vartheta}$ by inversion. However, there is an additional unknown, ψ_ϑ, which prohibits from directly inverting $\mathbf{C}$. However, when one pixel layer in the G_ϑ direction is omitted, and is void in terms of the imaged object, the inversion is possible. First, a new matrix, say $\tilde{\mathbf{C}}$ is constructed from $\mathbf{C}$ by removing its first column. Then the inversion is possible by

$$\mathbf{a}(p_\omega, q_\varphi) = (\tilde{\mathbf{C}}^T\tilde{\mathbf{C}})^{-1}\tilde{\mathbf{C}}^T\tilde{\mathbf{a}}(p_\omega, q_\varphi) , \quad (10)$$

where $\mathbf{a}(p_\omega, q_\varphi)$ is the same as $\tilde{\tilde{\tilde{\mathbf{a}}}}(p_\omega, q_\varphi)$, but with one less element. In the process of inversion, ψ_ϑ has to be evaluated. This can be done by iteration, wherein the similarity of $\tilde{\tilde{\mathbf{a}}}(p_\omega, q_\varphi)$ and $\tilde{\mathbf{C}}\mathbf{a}(p_\omega, q_\varphi)$ is used as a convergence criterion. Finally, the 3D magnitude image is represented by voxel values

$$I(p_\omega, q_\varphi, s_\vartheta) = \big|a(p_\omega, q_\varphi, s_\vartheta)\big| . \quad (11)$$

TABLE I

SIMULATION PARAMETERS. SEE TEXT FOR EXPLANATIONS.

f_s	10 kHz	FOV	$(20 \text{ cm})^3$
f_0	2 kHz	B_0	50 μT
P_ω	8	G_ω	7 μT/m
Q_φ	7	G_φ	13 μT/m
S_ϑ	6	G_ϑ	150 μT/m
T_E	130 ms	$t_{\text{acq.}}$	T_E
τ	$T_E/2$	$\frac{V_{\text{box}}}{\text{FOV}}$	$\frac{(P_\omega-2)(Q_\varphi-2)(S_\vartheta-2)}{P_\omega Q_\varphi S_\vartheta}$
T_2	30 – 100 ms	T_2^+	$0.4\,T_2$
L	~ 1 mH	I_ϑ	~ 5 A
PWR_ϑ	~ 300 W		

B. Simulations

The phantom simulations were performed with the parameters in Table I, without adding noise. The duration of the acquisition $t_{\text{acq.}}$; the duration of encodings τ; the approximate inductance of the gradient-excitation coil L; the maximum current needed to generate the gradient-excitation field, I_ϑ;
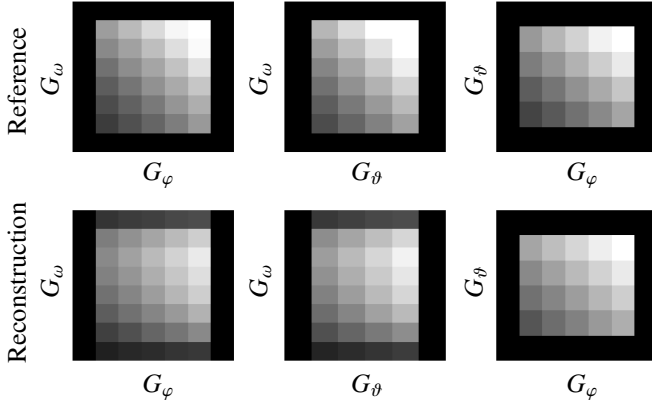
Fig. 3. Simulated phantom images at the centre planes of the imaged rectangular box. The encoding directions are: G_ω for frequency, G_φ for phase, and G_ϑ for gradient-excitation. The reference images were calculated by considering relaxation in each voxel; the reconstructed images were obtained by generating composite signals that could be physically detected, and following the reconstruction cascade presented in Methods. The images have the same gray scale. See Table I and Section II-B for further details.

the volume of the rectangular phantom box, V_{box}; and the maximum power required from the gradient-excitation power supply, PWR_ϑ, are given in the table. It should also be noted that G_φ and G_ϑ are maximum phase- and gradient-excitation-encoding amplitudes. The necessary bandwidth of the gradient-excitation pulse comes at an expense of growing pulse amplitude. The voxel-intensity variations were achieved by having inhomogeneous relaxation times within the imaged rectangular-box phantom. Within the FOV, the phantom had spin density $\rho(p_\omega, q_\varphi, s_\vartheta) = 1$, except at the voxels at the borders, where it was 0 (in the background). The relaxation times were set to be

$$
\begin{aligned}
T_2(p_\omega, q_\varphi, s_\vartheta) &= T_2(1,1,1) \\
&+ \frac{1}{3}\left[\frac{p_\omega - 1}{P_\omega - 1} + \frac{q_\varphi - 1}{Q_\varphi - 1} + \frac{s_\vartheta - 1}{S_\vartheta - 1}\right] \\
&\times [T_2(P_\omega, Q_\varphi, S_\vartheta) - T_2(1,1,1)] , \quad (12) \\
T_2^+(p_\omega, q_\varphi, s_\vartheta) &= 0.4\, T_2(p_\omega, q_\varphi, s_\vartheta) , \quad (13)
\end{aligned}
$$

where T_2 was minimum at $(1,1,1)$ and maximum at $(P_\omega, Q_\varphi, S_\vartheta)$ (see Table I for limits). The imaging sequence is sketched in Fig. 2.

III. RESULTS

The simulated images are shown in Fig. 3, with a phantom with uniform spin density and a uniform gradient in the relaxation times T_2 and T_2^+ from one corner of the rectangular box towards the opposite one, as in (12) and (13). The reference images were calculated from the average relaxation envelopes of (1) for each voxel. The reconstructed images were computed starting from (5), and using the presented reconstruction methods. It can be seen that the correspondence between the reconstructed and reference images is good. The slight blurring in the frequency-encoding direction G_ω is attributed to spectral leakage in the Fourier reconstruction because of the T_2 and T_2^+ relaxations. This can be seen

at the edges of the box where $p_\omega = 1$ or $p_\omega = P_\omega$. However, the relaxation-time gradients reproduce in both cases and in all planes. The power requirement for producing the gradient-excitation field, estimated at around 300 W, is sufficiently small for a real-world implementation of the imaging procedure. As a way to enable the new encoding method, it is suggested that the gradient-excitation waveform is both amplitude and frequency modulated.

IV. CONCLUSIONS

ULF MRI is a good application for the presented gradient-excitation encoding: because the Larmor frequencies are low, there is negligible signal attenuation through tissue and the pulses can be applied with relatively low-power amplifiers, *e.g.* audio amplifiers. Gradient-excitation encoding, together with frequency and phase encodings, can be combined in a new 3D image-reconstruction method. This was demonstrated by simulations; for a practical implementation, pulsed broadband gradient-excitation fields that are orthogonal to the measurement field are needed for each gradient-excitation step. It is suggested that the gradient-excitation pulse bandwidth could be enhanced with both amplitude and frequency modulations. To fix the one indeterminate phase variable in gradient excitation, one extra encoding step and one extra layer of empty volume outside the imaged object are required. The reconstructions were successful in all three encoding directions. Practical implementation of the method is left for future work.

REFERENCES

[1] J. Clarke, M. Hatridge, and M. Mößle, SQUID-detected magnetic resonance imaging in microtesla fields, Annu. Rev. Biomed. Eng., vol. 9, pp. 389–413, 2007.
[2] V. S. Zotev, A. M. Matlashov, P. L. Volegov, A. V. Urbaitis, M. A. Espy, and R. H. Kraus Jr., SQUID-based instrumentation for ultralow-field MRI, vol. 20, pp. S367-S373, 2007.
[3] M. Hämäläinen, R. Hari, R. J. Ilmoniemi, J. Knuutila, and O. V. Lounasmaa, Magnetoencephalography—theory, instrumentation, and applications to noninvasive studies of the working human brain, Rev. Mod. Phys., vol. 65, pp. 413–497, 1993.
[4] P. A. Bottomley and E. R. Andrew, RF magnetic field penetration, phase shift and power dissipation in biological tissue: Implications for NMR imaging, Phys. Med. Biol., vol. 23, pp. 630–643, 1978.
[5] P. E. Magnelind, J. J. Gomez, A. N. Matlashov, T. Owens, J. H. Sandin, P. L. Volegov, and M. A. Espy, Co-registration of interleaved MEG and ULF MRI using a 7 channel low-T_c SQUID system, IEEE Trans. Appl. Supercond., vol. 21, pp. 456–460, 2011.

[6] P. T. Vesanen, J. O. Nieminen, K. C. J. Zevenhoven, J. Dabek, L. T. Parkkonen, A. V. Zhdanov, J. Luomahaara, J. Hassel, J. Penttilä, J. Simola, A. I. Ahonen, J. P. Mäkelä, and R. J. Ilmoniemi, Hybrid ultra-low-field MRI and MEG system based on a commercial whole-head neuromagnetometer, submitted, 2012.

[7] J. O. Nieminen, M. Burghoff, L. Trahms, and R. J. Ilmoniemi, Polarization encoding as a novel approach to MRI, J. Magn. Reson., vol. 202, pp. 211–216, 2010.

[8] J. B. Weaver, Y. Xu, D. M. Healy, and J. R. Driscoll, Wavelet-encoded MR imaging, Magn. Reson. Med., vol. 24, pp. 275–287, 1992.

[9] G. P. Zientara, L. P. Panych, and F. A. Jolesz, Dynamically adaptive MRI with encoding by singular value decomposition, Magn. Reson. Med., vol. 32, pp. 268–274, 1994.

[10] J. C. Sharp and S. B. King, MRI using radiofrequency magnetic field phase gradients, Magn. Reson. Med., vol. 63, pp. 151–161, 2010.

[11] P. T. Vesanen, J. O. Nieminen, K. C. J. Zevenhoven, J. Dabek, J. Simola, J. Sarvas, and R. J. Ilmoniemi, The spatial and temporal distortion of magnetic fields applied inside a magnetically shielded room, IEEE Trans. Magn., vol. 48, pp. 53–61, 2012.

[12] J. O. Nieminen, P. T. Vesanen, K. C. J. Zevenhoven, J. Dabek, J. Hassel, J. Luomahaara, J. S. Penttilä, and R. J. Ilmoniemi, Avoiding eddy-current problems in ultra-low-field MRI with self-shielded polarizing coils, J. Magn. Reson., vol. 212, pp. 154–160, 2011.

[13] J. Luomahaara, P. T. Vesanen, J. Penttilä, J. O. Nieminen, J. Dabek, J. Simola, M. Kiviranta, L. Grönberg, C. J. Zevenhoven, R. J. Ilmoniemi, and J. Hassel, All-planar SQUIDs and pickup coils for combined MEG and MRI, Supercond. Sci. Tech., vol. 24, 075020, 2011.

[14] D. I. Hoult, Rotating frame zeugmatography, J. Magn. Reson., vol. 33, pp. 183–197, 1979.

[15] J. Dabek, P. T. Vesanen, K. C. J. Zevenhoven, J. O. Nieminen, R. Sepponen, and R. J. Ilmoniemi, SQUID-sensor-based ultra-low-field-MRI calibration with phantom images: Towards quantitative imaging, submitted, 2012.

[16] V. S. Zotev, A. N. Matlashov, I. M. Savukov, T. Owens, P. L. Volegov, J. J. Gomez, and M. A. Espy, SQUID-based microtesla MRI for in vivo relaxometry of the human brain, IEEE Trans. Appl. Supercond., vol. 19, pp. 823–826, 2009.

[17] J. Pauly, P. Le Roux, D. Nishimura, and A. Macovski, Parameter relations for the Shinnar–Le Roux selective excitation pulse design algorithm, IEEE Trans. Med. Imag., vol. 10, pp. 53–65, 1991.

[18] M. A. Janich, R. F. Schulte, M. Schwaiger, and S. J. Glaser, Robust slice-selective broadband refocusing pulses, J. Magn. Reson., vol. 213, pp. 126-135, 2011.